

Codoping Mg-Mn Based Oxygen Carrier with Lithium and Tungsten for Enhanced C_2 Yield in a Chemical Looping Oxidative Coupling of Methane SystemDeven S. Baser,[§] Zhuo Cheng,[§] Jonathan A. Fan, and Liang-Shih Fan*Cite This: *ACS Sustainable Chem. Eng.* 2021, 9, 2651–2660

Read Online

ACCESS |



Metrics & More



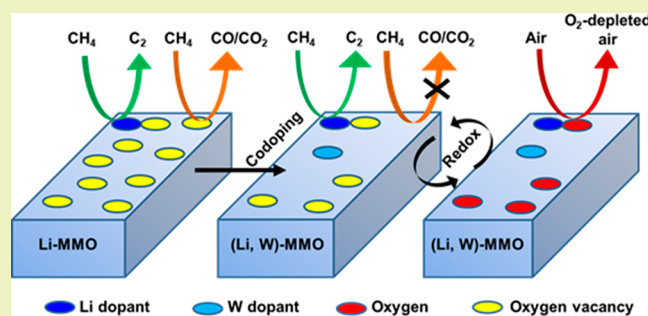
Article Recommendations



Supporting Information

ABSTRACT: Oxidative coupling of methane (OCM) is a compelling strategy for the direct conversion of methane to C_{2+} hydrocarbons in order to produce fuels and value-added chemicals. Nevertheless, it remains challenging to achieve the high C_{2+} yield that is desirable in industrial synthesis. Here, a lithium, tungsten-codoped Mg-Mn based oxygen carrier, (Li,W)- Mg_6MnO_8 , is prepared for the chemical looping oxidative coupling of methane (CLOCM) technology. The designed codoped oxygen carrier exhibits an improved OCM performance with a C_{2+} yield of 28.6% at 850 °C, which is 80% higher than the combined yields of the single Li- and W-doped oxygen carriers, and 330% higher than that of the undoped Mg_6MnO_8 oxygen carrier. The enhanced activity has also been demonstrated over 50 redox cycles in the CLOCM system. In combination with solid characterization, density functional theory calculations reveal that, as compared to the single-metal-doped Mg_6MnO_8 , the Li and W codopants work synergistically which not only enhances CH_3 dimerization but also inhibits CO_2 formation. This effect was attributed to the suppressed formation of unselective oxygen vacancies, which in turn leads to the C_{2+} yield enhancement. As a result, (Li,W)- Mg_6MnO_8 was found to be one of the best performing oxygen carriers as compared to other oxygen carriers reported in the literature. These findings provide new insights into the understanding of the codoping effect on the activity of a Mg-Mn based oxygen carrier for C_{2+} production and can open new avenues to design an environmentally and economically feasible CLOCM system.

KEYWORDS: Chemical looping, Oxidative coupling of methane, Oxygen carrier, Redox reaction, Synergistic effect



INTRODUCTION

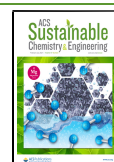
Recent discoveries of CH_4 reserves in the form of shale gas have caused a resurgence of technologies that convert CH_4 to value added products.^{1,2} Certain reserves, which amount to a considerable portion of the worldwide CH_4 resource, suffer from monetization issues due to their distance from the market and are termed as stranded CH_4 reserves.^{3,4} As the commercially available indirect CH_4 valorization technologies rely on economy of scale to be feasible, the CH_4 generated from these small and low value stranded reserves is often flared, generating CO_2 .^{5,6} It has caused a sustainability problem, where not only is the CH_4 resource being lost but also the act of flaring puts a CO_2 footprint on the process. Thus, technologies that are more effective at converting CH_4 to products are crucial, with the world heading toward reducing greenhouse emissions.^{7,8} Specifically, technologies related to the direct conversion of CH_4 to chemicals have gained momentum as it simplifies the overall process, leading to reduced costs and improved energy efficiencies.^{1,9–11} The CH_4 sources can range from stranded natural gas, associated gas, to bio-derived methane where the chemicals synthesized in

these direct utilization of CH_4 technologies range from aromatics, olefins, to oxygenates such as methanol.^{12–20} Among these technologies, oxidative coupling of methane (OCM) has been shown to have the highest estimated kinetic yield.^{1,21} Under OCM, CH_4 is converted to C_{2+} hydrocarbons in a single step, typically over a catalyst and in the presence of an oxygen species, O_2 . Here, C_{2+} refers to C_2 's such as ethane and ethylene and higher hydrocarbons. However, the oxidation of CH_4 to CO and CO_2 competes with the CH_3 radical coupling to C_{2+} , imposing limitations to the selectivity of the desired hydrocarbon products. In addition, the over-oxidation of the desired products such as ethane/ethylene is much more favorable as compared to CH_4 .²² This results in an upper limit

Received: September 30, 2020

Revised: January 8, 2021

Published: February 9, 2021



for the overall yield for a catalytic OCM system at 25%,²³ where the economically feasible overall yield is estimated to be greater than 30%.^{24,25} The need to address these challenges has driven the development of novel systems and unique OCM catalyst designs.^{26–28}

The chemical looping oxidative coupling of methane (CLOCM) is a promising alternative approach in comparison to the catalytic mode for C_{2+} production. Instead of cofeeding O_2 with CH_4 over a catalyst, CLOCM utilizes the lattice oxygen from a reducible metal oxide or a catalytic oxygen carrier as the oxygen source for the OCM reaction. Figure 1 depicts the reaction scheme of CLOCM where the

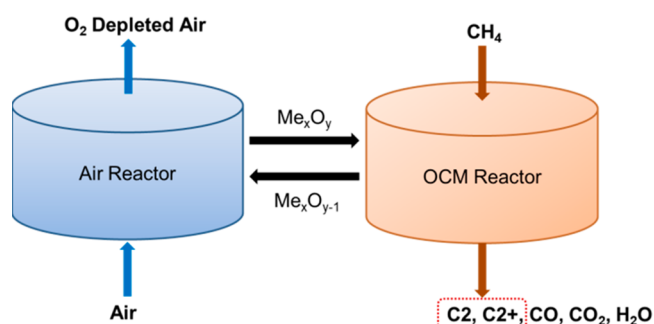


Figure 1. Schematic representation for the chemical looping oxidative coupling of methane (CLOCM).

metal oxide/catalytic oxygen carrier provides the active sites for the conversion of methane to C_2/C_{2+} hydrocarbon products and H_2O in the OCM reactor. The reduced catalytic oxygen carrier, upon oxygen donation from the OCM reactor, can be regenerated by air in a separate reactor (air reactor) to complete a full cycle of the redox reaction. This change of oxygen source as compared to the catalytic system eliminates the use of an air separation unit, which is an energy and cost intensive unit operation.^{25,31} Further, due to the absence of O_2 in the gas phase, the CLOCM system gets rid of unwanted gas-phase reactions, potentially raising the cap on the C_{2+} yield that can be achieved through OCM.^{32,33}

Despite these advantages, the reported catalytic oxygen carriers for CLOCM have yet to show exceptional performance as compared to the catalytic OCM. Here, a higher performance in the form of high C_{2+} selectivity along with a high CH_4 conversion would provide not only the most economically feasible system but also the most sustainable system in terms of carbon efficiency toward the products. Statistical analysis on such strategies has suggested an ideal recipe for an OCM catalyst, where the catalyst's components work synergistically to provide an optimal yield; however, such a catalyst has not been synthesized yet.²² Figure 2 shows a quantitative comparison between the C_{2+} generation performance of different oxygen carriers through CLOCM, where a majority of the CLOCM systems operate with a C_{2+} yield of <25%. Over these catalytic oxygen carriers and catalysts from the traditional OCM system, the commonly accepted mechanism for OCM is the generation of CH_3 radicals through CH_4 activation on surface active sites where the radicals eventually couple to form C_2 hydrocarbons.^{27,34,35} These active sites have been induced by doping alkali metal oxides/chlorides or transition state metal oxides,^{36–38} forming mixed metal oxides,^{39,40} addition of inert support materials, etc.,^{41,42} to maximize the C_2 and C_{2+} yields. It is important to note that

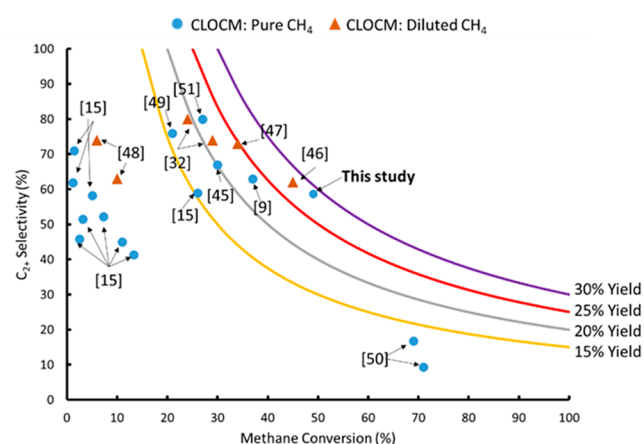


Figure 2. Comparison of CLOCM systems on a C_{2+} selectivity vs CH_4 conversion plot from the literature and this work.^{9,15,52,32,45–51}

there are two categories of data that differ in the experimental methodology that was used to collect the data. The blue circles represent the performance of the oxygen carriers when it was reduced under pure CH_4 and the orange triangles represent the performance of the oxygen carriers that had a pulsed CH_4 injection under a constant inert carrier gas flow. The latter methodology is useful in capturing the time-evolving features in the product distribution, giving insights about the reaction mechanism. However, the performance that this methodology captures skews the data due to the dilution effect of the inert carrier gas, displaying a higher selectivity than what would be observed with pure CH_4 .^{43,44} Thus, from a commercially relevant standpoint, the goal of this study was to design an oxygen carrier that displays a high C_{2+} yield under the pure CH_4 condition.

The Mg–Mn composite material, Mg_6MnO_8 , has been proven to be suitable for CLOCM due to its stable reactivity toward hydrocarbon synthesis over multiple redox cycles and its high oxygen release capacity.^{20,53} In this work, the C_{2+} formation over Mg_6MnO_8 oxygen carriers with a low concentration of Li and W dopants in the CLOCM system was comprehensively investigated. (Li,W)-codoped Mg_6MnO_8 has unique properties that are driven by synergy between the dopants and thus distinguished from the singly doped Mg_6MnO_8 in the aspect of oxygen vacancy formation. The codoping-induced oxygen vacancies dramatically facilitate CH_4 dissociation and CH_3 dimerization, leading to a C_{2+} yield of 28.6%, which is by far the highest in CLOCM systems, as shown in Figure 2. This work will provide insights into effective oxygen carrier design and have broader impacts on the development of an environmentally and economically feasible CLOCM technology.

EXPERIMENTAL SECTION

Catalytic Metal Oxide Synthesis and Characterization. For this study, Li-doped Mg_6MnO_8 (Li- Mg_6MnO_8), W-doped Mg_6MnO_8 (W- Mg_6MnO_8), and four (Li,W)-codoped Mg_6MnO_8 with varying ratios of Li and W were synthesized. For the single dopant Mg_6MnO_8 , stoichiometric quantities of MnO_2 (Materion, 99.9% pure), MgO (Materion, 99.9% pure), and the respective dopant (2.65% mol) were hand ground with 50 wt % DI water. For synthesizing Li- Mg_6MnO_8 , LiOH (Sigma-Aldrich, 98% pure) was used, and for W- Mg_6MnO_8 , WO_3 (Alfa Aesar, 99.9% pure) was used. The four (Li,W)-codoped catalytic metal oxides were also synthesized in a similar fashion, with the dopant composition of Li and W varied in combinations of 2.65%

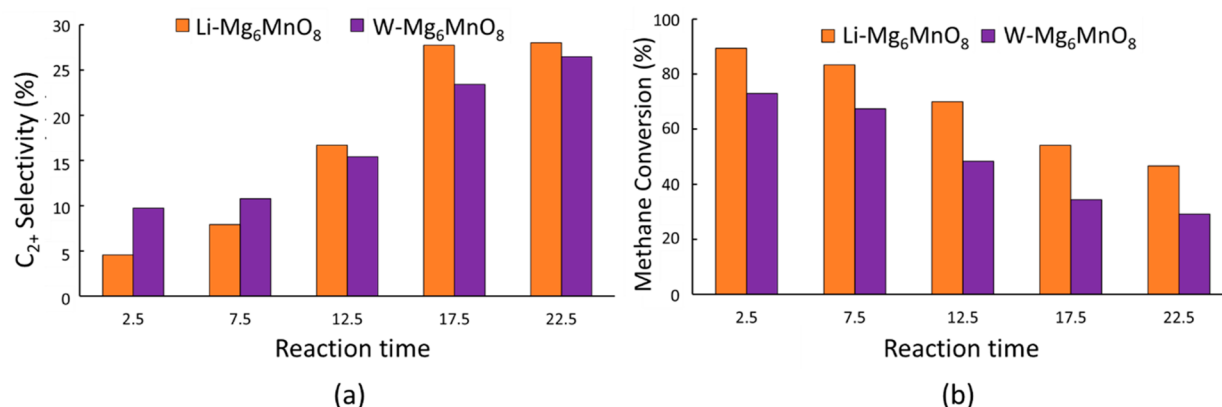


Figure 3. (a) C₂₊ selectivity versus reaction time for Li-Mg₆MnO₈ and W-Mg₆MnO₈ and (b) methane conversion versus reaction time for Li-Mg₆MnO₈ and W-Mg₆MnO₈ at 850 °C and 1 atm at a GHSV of 2400 h⁻¹.

and 4%. All the doped samples were calcined under air at 950 °C for 8 h. All of these catalytic oxygen carriers were ground and sieved post-calcination to a size of 300–850 μm.

H₂-temperature programmed reduction (H₂-TPR) was used to characterize the reducibility of the oxygen carrier. Here, the metal oxide sample is subjected to a H₂ containing environment, where the sample reacts with H₂ as the reaction temperature is increased linearly. These experiments are carried out in a thermogravimetric analyzer, which measures the weight of the metal oxide sample as it undergoes reduction. The negative derivative of that weight with temperature is plotted against the reaction temperature to get the reduction profile. The hydrogen concentration used in these experiments is 50% vol with balance N₂. The temperature ramp rate was 10 °C/min and was kept constant across the different runs.

The samples were also analyzed in a Kratos axis ultra XPS with monochromated aluminum source X-rays for scanning the samples. The instrument was run with an accelerating voltage of 12 kV and filament current of 10 mA. A charge neutralizer was used with the filament current at 2.2 A and the charge balance at 2.5 V. Additionally, the scanning electron microscope (SEM) was used to obtain images of the surface morphology before and after redox cycles. The SEM was operated with a 20 kV and a 43 pA electron beam.

Fixed Bed Setup for Simulated Chemical Looping Tests.

Redox experiments were carried out in a fixed bed reactor system, which has been illustrated in previous studies and in Figure S1a.^{9,50} The OCM reaction was carried out for 15 s or 30 s with pure CH₄ with a flow of 200 mL/min, and the air re-oxidation was carried out for 30 min with air flowing at 200 mL/min. A N₂ purge of 10 min at 200 mL/min was run between the reduction and oxidation steps to avoid the formation of any explosive mixtures. The oxidation time was kept excessively long based on a previous study⁵⁰ which ensured that the oxygen carrier was completely re-oxidized and carbon deposited on the carrier, if any, was burnt off. This cyclic operation is illustrated in Figure S1b, where one fixed bed reactor can be operated in a simulated chemical looping fashion. Gas analysis was done by a gas chromatography analyzer (Agilent GC 8900B) or a Fourier Transform Infrared gas analyzer (CAI 6000 FTIR). For the gas chromatography analyzer, gas bags were used to capture the gas samples which were injected into the analyzer through a gas syringe. The FTIR was an online gas analyzer operated at 191 °C with a heated line into the analyzer operated at 200 °C. The performance of the different variations of the doped Mg₆MnO₈ catalytic oxygen carriers was examined through CH₄ conversion (eq S1) and C₂₊ selectivity (eq S2) performance metrics given in eqs S1 and S2 depicted in the Supporting Information.

Density Functional Theory (DFT) Calculations. The first-principles calculations were performed within the framework of density functional theory (DFT), using the Vienna Ab initio Simulation Package (VASP).^{54,55} The generalized gradient approximation of Perdew, Burke, and Ernzerhof⁵⁶ was used to represent the

exchange-correlation energy with details of the calculations illustrated in the Supporting Information. For the activation and dissociation barrier calculations, the climbing-image nudged elastic band (CI-NEB) method was used.

RESULTS AND DISCUSSION

Effect of Single Dopants on Mg₆MnO₈ in the CLOCM System. With the goal to study the codoping effect of Li and W and characterize any potential synergy between the two dopants on the C₂₊ yield, Li-doped Mg₆MnO₈ (Li-Mg₆MnO₈) and W-doped Mg₆MnO₈ (W-Mg₆MnO₈) samples were first synthesized and their performance was analyzed. The individually doped catalytic oxygen carriers would provide the baseline activity data that will be later compared with the (Li,W)-codoped catalytic oxygen carrier. Both the metal oxide composites were tested in the fixed bed reactor. The catalytic oxygen carrier reduction reaction in the fixed bed reactor was carried out for 30 s at 850 °C for Li- and W-doped Mg₆MnO₈ with the gas sample bagged every 5 s. The gas residence time of the reactor system is 5 s as tested from blank runs. The X-axis in Figure 3a,b depicts the average time for each bag, excluding the first 5 s of the reduction which can be ignored due to the gas residence time. However, it was found that catalytic oxygen carrier reduction for 30 s can lead to carbon deposition at the end of the reduction step, so the reduction time for the (Li,W)-codoped Mg₆MnO₈ sample was reduced to 15 s. This precautionary step was undertaken to prevent any loss in activity over cycles due to carbon deposition.

Panels (a) and (b) in Figure 3 depict the C₂₊ selectivity and CH₄ conversion profile for Li- and W-Mg₆MnO₈ catalytic oxygen carriers, respectively. Both the oxygen carriers show a characteristic trend seen in CLOCM systems that are operated in a fixed bed.^{9,15,45} Initially, as CH₄ is fed over the oxidized catalytic oxygen carrier, the CH₄ conversion is high due to the high concentration of lattice oxygen available for the CH₄ to react. Consequently, this also leads to over-oxidation of CH₄ and the C₂₊ products, which is seen as a low C₂₊ selectivity initially. As the OCM reaction progresses, the lattice oxygen is abstracted by CH₄ and the oxygen concentration of the oxygen carrier decreases as it gets reduced. This results in a reduction of CH₄ conversion and also reduces the over-oxidation tendency, thus improving the C₂₊ selectivity. While comparing the two dopants, W-Mg₆MnO₈ shows a higher C₂₊ selectivity than the Li-doped counterpart until 7.5 s. However, the C₂₊ selectivity of the Li-Mg₆MnO₈ is higher after 12.5 s, indicating a more selective nature of Li than W toward C₂₊ hydrocarbon

production. Additionally, the CH_4 conversion is higher for $\text{Li-Mg}_6\text{MnO}_8$ than the $\text{W-Mg}_6\text{MnO}_8$ throughout the reaction time. Upon comparing the OCM activity of both the dopants, it can be concluded that the W doping reduced the tendency of the oxygen carrier to donate oxygen to CH_4 as compared to the Li-doped metal oxide. In other words, the tendency for oxygen vacancy formation is lower for the $\text{W-Mg}_6\text{MnO}_8$ which is indicated by its lower CH_4 conversion than $\text{Li-Mg}_6\text{MnO}_8$ as seen in Figure 3b. Thus, as the lattice oxygen is more strongly bound for the $\text{W-Mg}_6\text{MnO}_8$ as compared to the $\text{Li-Mg}_6\text{MnO}_8$, the over-oxidation tendency of the W-doped sample reduces. This phenomenon is highlighted in the C_{2+} selectivity plot in Figure 3a where the first 7.5 s indicates a lower over-oxidation potential or a higher C_{2+} selectivity for the $\text{W-Mg}_6\text{MnO}_8$ as compared to $\text{Li-Mg}_6\text{MnO}_8$. Hereafter, as the catalytic oxygen carrier reduction proceeds, the surface oxygen vacancy concentration increases. Here, the effect of Li dopant induced oxygen vacancy on the OCM reactions translates to a higher C_{2+} selectivity post 7.5 s in the reduction step as compared to the $\text{W-Mg}_6\text{MnO}_8$ catalytic oxygen carrier.

Effect of Li and W Codoping on Mg_6MnO_8 in the CLOCM System. (Li,W)- Mg_6MnO_8 samples were synthesized to investigate the codoping effect on the OCM activity based on the method outlined in the Experimental Section. Different compositions of the two dopants were tested against their OCM activity to ascertain the optimum composition that provided the highest C_{2+} yield. Here, the C_{2+} yield was calculated as an average over the entire OCM reaction period of 15 s. It was found that Mg_6MnO_8 with 2.65% Li and 4% W dopant quantity exhibited the highest C_{2+} yield as shown in Figure S2. In Figure 4a, the OCM activity of the optimized (Li,W)-codoped oxygen carrier is illustrated with respect to reaction temperature. The optimum composition for the codoped sample gave an overall hydrocarbon yield of 28.6% at 850 °C. Here, the overall hydrocarbon yield includes C_2 's and higher hydrocarbons (C_{3+}) over the entire OCM reaction period of 15 s. As seen in Figure 4a, the methane conversion improved and the C_2+C_{3+} selectivity dropped with an increase in the reaction temperature. This can be attributed to the increase in the over-oxidation tendency with the increase in the reaction temperature. In other words, as temperature increased, the kinetics of methane reacting with the catalytic oxygen carrier increased, thus improving the CH_4 conversion. On the other hand, the kinetics for the subsequent undesired oxidation of C_{2+} products also improved with increasing temperature, thus converting the desired hydrocarbons into CO_x products. This inverse relationship between C_{2+} selectivity and CH_4 conversion creates a volcano plot for the overall hydrocarbon yield with its optima at 850 °C as seen in Figure S3.

Apart from the formation of CO_x due to successive oxidation reactions, other gas phase reactions can also shape the final distribution of the products. CH_3 dimerization leads to the formation of C_2H_6 , which can either thermally or oxidatively dehydrogenate to form C_2H_4 . The thermal decomposition of C_2H_6 to C_2H_4 increases with increasing temperature as the higher temperature favors the C–H bond scission than the C–C bond scission.⁵⁷ Thus, the $\text{C}_2\text{H}_4/\text{C}_2\text{H}_6$ ratio increases with increasing reaction temperature in the CLOCM system as seen in Figure 4b. Further, the addition of CH_3 radicals to the C_2 products leads to the formation of C_{3+} products. Because of the abundance of CH_3 radicals with increasing temperature and the lack of molecular oxygen that can over-oxidize any higher

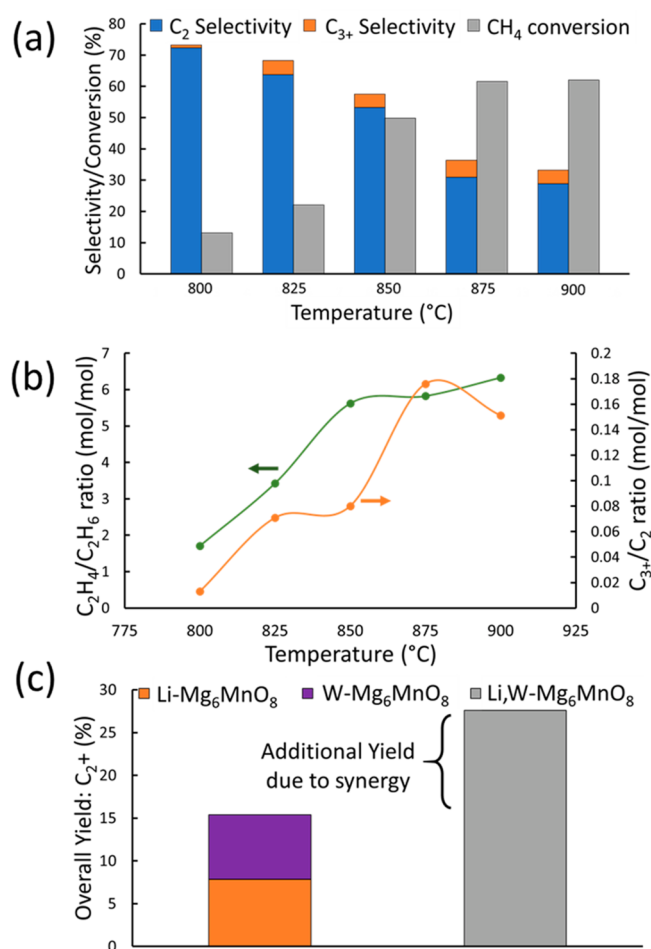


Figure 4. (a) C_2 selectivity, C_{3+} selectivity, and methane conversion versus temperature for (Li,W)- Mg_6MnO_8 , (b) effect of temperature on the $\text{C}_2\text{H}_4/\text{C}_2\text{H}_6$ ratio, depicted by the green curve, and C_{3+}/C_2 ratio over (Li,W)- Mg_6MnO_8 , depicted by the orange curve, and (c) comparison of the combined overall yield of $\text{Li-Mg}_6\text{MnO}_8$ and $\text{W-Mg}_6\text{MnO}_8$ and the overall yield of (Li,W)- Mg_6MnO_8 at 850 °C and 1 atm at a GHSV of 2400 h^{-1} . The yields were calculated based on the average C_{2+} selectivity and CH_4 conversion over 15 s of Li- and W-doped Mg_6MnO_8 samples.

hydrocarbons, the C_{3+} hydrocarbon formation with respect to C_2 hydrocarbon products increases with increasing temperature, as seen in Figure 4b. However, the dip in the trend at 900 °C can be attributed to cracking reactions, favoring smaller chain hydrocarbons as opposed to higher hydrocarbons. Finally, the synergy between the two dopants can be visualized from Figure 4c, where the overall yield of (Li,W)- Mg_6MnO_8 is 80% higher than the total combined overall yields of Li- and W-doped samples. Further, the reported yield on an undoped Mg_6MnO_8 is 6.7%,⁵⁰ where the codoping strategy enhances the overall yield by 330% to 28.6% at 850 °C.

Solid Characterization of the Li and W-Codoped Mg_6MnO_8 . To further understand the nature of the codoping effect, H_2 -temperature programmed reduction (H_2 -TPR) was used to investigate the reducibility of the undoped and doped Mg_6MnO_8 . H_2 -TPR reduction profiles, as seen in Figure 5, display the reduction potential of the metal oxide as it goes through several solid oxide phases during reduction. The details of the H_2 -TPR operation have been provided in the Experimental Section.

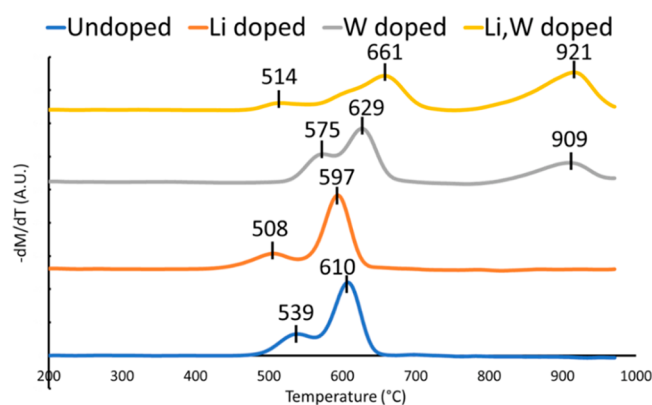


Figure 5. H_2 -temperature programmed reduction (H_2 -TPR) profiles for the undoped Mg_6MnO_8 , Li- Mg_6MnO_8 , W- Mg_6MnO_8 , and (Li,W)-codoped Mg_6MnO_8 .

In H_2 -TPR, if the temperature corresponding to the maxima of the peak shifts to the left, i.e., to a lower temperature, it signifies an ease of reduction. In other words, a peak at a lower temperature has a higher over-oxidation potential toward hydrocarbons/reducing gases than a peak at a higher temperature and vice versa. A higher over-oxidation potential corresponds to the metal oxide showing higher CH_4 conversion tendency, which can also have the potential to reduce the hydrocarbon selectivity. However, hydrocarbon selectivity also depends on the active sites present on the metal oxide surface and thus does not have a direct correlation with the H_2 -TPR reduction profiles. The undoped Mg_6MnO_8 sample was kept as a basis for comparing the trends seen for the three doped samples. The Li-doped sample shows a shift toward the left and the W-doped sample shows a shift to the right, as compared to the undoped sample. This corroborates the data seen in Figure 3b which shows higher CH_4 conversion for Li- Mg_6MnO_8 as compared with W- Mg_6MnO_8 . On the other hand, the hydrocarbon selectivity also increases due to the Li dopant induced oxygen vacancies.⁵⁰ The W-doped sample has an additional peak at $\sim 909^\circ\text{C}$ as compared to the undoped and the Li-doped sample, which corresponds to the reduction of W^{6+} . The (Li,W)-codoped sample shows a peculiar reduction profile as compared to the Li- and W-doped

samples. The peak corresponding to Mn^{3+} to Mn^{2+} shifts to the right, where the temperature of reduction increases from 610 to 661°C as compared to the undoped sample. This results in the CH_4 conversion being in between the undoped and the W-doped sample. Also, the peak corresponding to the reduction of W^{6+} shifts to the left as compared to the W-doped sample. Both of these peak shifts indicate an interaction between the Li dopant and the W dopant, where the effect on the Li dopant is much more pronounced. This interaction between the two dopants is what helps in synergistically combining the properties to the two dopants on Mg_6MnO_8 .

The XPS data from Figure 6a–c give the surface composition and the oxidation states of the respective species present on the codoped sample. The XPS spectra of Mg 2s depict a +2 oxidation state of Mg on the surface as depicted by Figure 6a. Further, Figure 6b portrays the multiplet splitting of the Mn $2p_{3/2}$ peak represents Mn in its +4 oxidation state.⁵⁸ Figure 6c corresponds to W on the surface in a +6 oxidation state.⁵⁹ The spectrum for Li was not noticeable at these low concentrations as the sensitivity of Li is lower than other metals for XPS. However, as seen from the H_2 -TPR, both Li and W dopants interact with each other in the codoped sample, and thus Li should also be present with W on the surface of the catalytic oxygen carrier. No significant differences were observed when comparing the XPS spectra of the codoped sample with the spectra of Li- Mg_6MnO_8 ⁵⁰ and W- Mg_6MnO_8 , which is illustrated in Figure S4.

Mechanism Studies of CLOCM. In order to explore the mechanism of CLOCM over doped Mg_6MnO_8 oxygen carriers, DFT calculations were performed. On the basis of our previous study,⁵⁰ the (111) surface of Mg_6MnO_8 was chosen as the slab model with a Mg-Mn outermost layer which was labeled as the s layer. Li- Mg_6MnO_8 with the $\text{Li}_{(s)}\text{-O}$ active site was built by replacing one magnesium atom in the s layer with one lithium atom. For the W dopant, its position at the top surface layer was found to be energetically more preferred than that in the subsurface by -0.24 eV. Therefore, one Mn atom at the s layer was substituted with W to build the W- Mg_6MnO_8 which includes the active site $\text{W}_{(s)}\text{-O}$. To model the codoping catalytic oxygen carrier, one Mg atom in W- Mg_6MnO_8 was substituted with the Li dopant. The optimized structures of Li-doped, W-doped, and Li,W-codoped Mg_6MnO_8 (111) slabs are

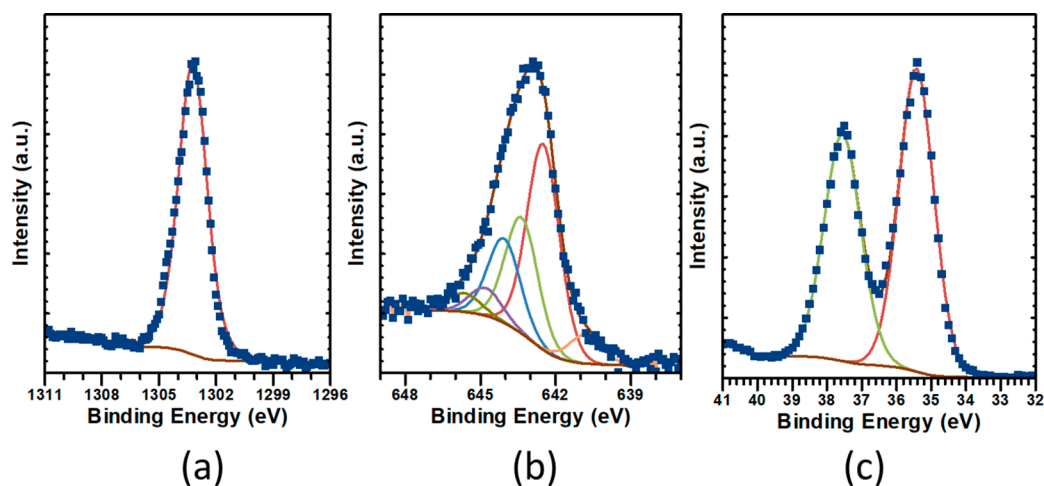


Figure 6. XPS spectra and the respective components for (a) Mg 2s, (b) Mn $2p_{3/2}$, and (c) W 4f in the fresh (Li,W)-codoped Mg_6MnO_8 catalytic oxygen carrier.

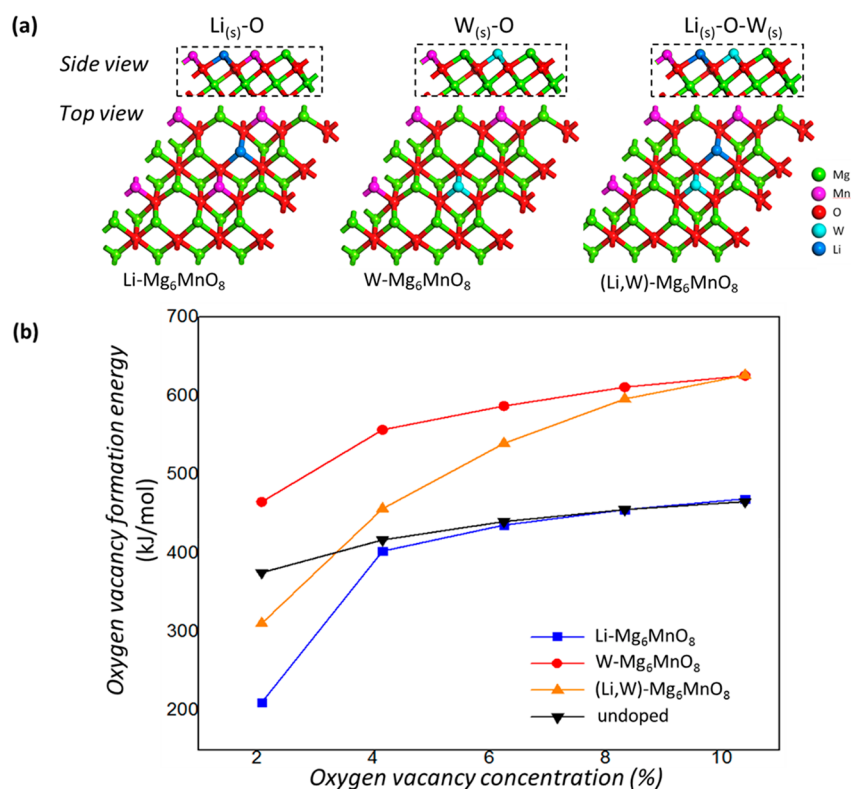


Figure 7. (a) Top view of the optimized structures of the $\text{Mg}_6\text{MnO}_8(111)$ slab with the Li dopant, W dopant, and (Li,W) dopant (side view of the structure is shown in the inset), (b) the oxygen vacancy formation energy (kJ/mol) plotted as a function of the oxygen vacancy concentration (%).

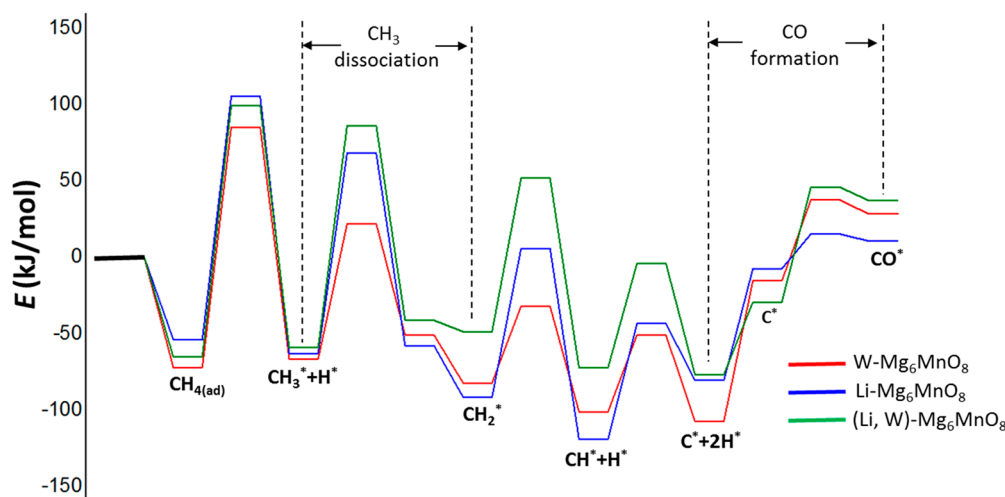


Figure 8. Energy profiles for CH_4 dissociation and CO^* formation on active sites of $\text{Li-Mg}_6\text{MnO}_8$, $\text{W-Mg}_6\text{MnO}_8$, and $(\text{Li,W})-\text{Mg}_6\text{MnO}_8$.

shown in Figure 7a. On the basis of the experimental and H_2 -TPR results, it was known that Li, W, and Li-W codoping have a different effect on the reducibility of Mg_6MnO_8 , which is crucial to its activity for CLOCM. Thus, to understand this phenomenon further, the tendency for the oxygen vacancy formation on these surfaces was investigated. The oxygen vacancy was created by removing a 5-fold coordinated lattice oxygen atom in the subsurface. The computed oxygen vacancy formation energies (E_f) as a function of oxygen vacancy concentration are shown in Figure 7b. It can be seen that E_f generally increases with an increase in the oxygen vacancy concentration. The E_f of $\text{Li-Mg}_6\text{MnO}_8$ increases to 469 kJ/mol

from 210 kJ/mol when the oxygen vacancy concentration increases to about 10%. For $\text{W-Mg}_6\text{MnO}_8$, the formation energy of the initial oxygen vacancy is 465 kJ/mol , which is 155 kJ/mol higher than that in $(\text{Li,W})-\text{Mg}_6\text{MnO}_8$. However, when the oxygen vacancy concentration reaches 8.3%, the E_f of $\text{W-Mg}_6\text{MnO}_8$ is only 15 kJ/mol higher than the E_f of $(\text{Li,W})-\text{Mg}_6\text{MnO}_8$. These results indicate that the W doping induces higher oxygen vacancy formation energy than that in undoped Mg_6MnO_8 and $\text{Li-Mg}_6\text{MnO}_8$. Thus, adding W dopant can inhibit the formation of a surface oxygen vacancy on Mg_6MnO_8 . In contrast, the Li doping does not significantly affect the formation energy of an oxygen vacancy on the

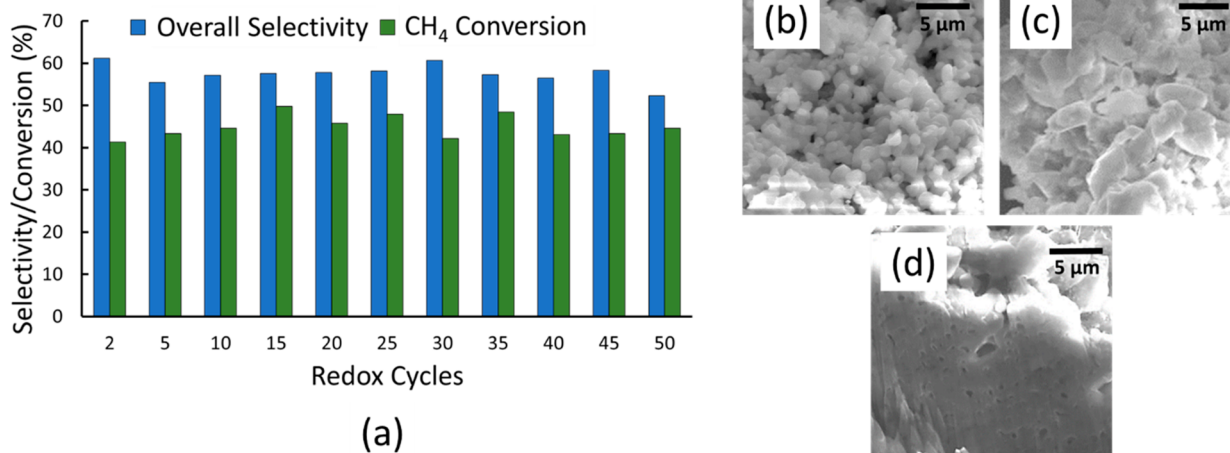


Figure 9. (a) Overall selectivity and methane conversion at 850 °C and 1 atm at a GHSV of 2400 h⁻¹ across 50 redox cycles for (Li,W)-Mg₆MnO₈ with 15 s of OCM reaction time; SEM images of (b) fresh (Li,W)-codoped Mg₆MnO₈, (c) 50 cycle (Li,W)-codoped Mg₆MnO₈, and (d) cross section of 50 cycle (Li,W)-codoped Mg₆MnO₈.

surface when the oxygen vacancy concentration is greater than 4%. The oxygen vacancy formation energy for (Li,W)-Mg₆MnO₈ mimics the lower energy requirement for oxygen vacancy formation at lower oxygen vacancy concentrations as the Li dopant and the higher oxygen vacancy formation energy as the W dopant at higher oxygen vacancy concentrations. Therefore, Li and W codoping not only induces the formation of an active site for CH₄ activation and dissociation but also suppresses CH₃ radical over-oxidation by stabilizing the surface lattice oxygen.

In order to further identify the synergetic effect of the codoping on the C₂₊ yield enhancement, the overall reaction profiles of the CH₄ dissociation, CH₃ radical formation, and the CO formation on the active sites of Li-Mg₆MnO₈, W-Mg₆MnO₈, and (Li,W)-Mg₆MnO₈ surfaces were investigated using the climbing-image nudged elastic band (CI-NEB) method,⁶⁰ as shown in Figure 8. After the CH₄ adsorption step, CH₄ dissociates to a CH₃ radical. The CH₃ radical can then desorb into the gas phase or further dissociate on the surface via C-H cleavage. It was found that CH₃ adsorption energies on Li(s)-O, W(s)-O, and Li(s)-O-W(s) are 111, 98, and 78 kJ/mol, respectively. This indicates that the Li and W-codoping induced Li(s)-O-W(s) active sites can destabilize the adsorbed CH₃ radicals more efficiently than the individual dopants. The desorbed CH₃ radicals enter the gas phase where CH₃ dimerization takes place to form C₂ hydrocarbons.

An alternative pathway for the CH₃ radical evolution is CH₃ dissociation to the methylene radical CH₂, which will lead to a decrease in C₂ yield. During this process, the CH₂ radical remains at the doping site when the extracted hydrogen migrates to the surface O site. The calculations show that the barrier of CH₃ dissociation on the Li(s)-O-W(s) site is 146 kJ/mol which is 14 kJ/mol higher than that on the Li(s)-O site, and 57 kJ/mol higher than that on the W(s)-O site. This reveals that the Li and W codoping inhibits the undesired C–H bond activation. The Li(s)-O-W(s) site also exhibits low activity for CH₂ dissociation due to the higher barrier, compared to the Li(s)-O site and W(s)-O site. In addition, the calculations also show that the Li(s)-O-W(s) site is unfavorable for CO formation because it needs to overcome a high energy barrier of 75 kJ/mol. In contrast, CO formation on the Li(s)-O and W(s)-O site is more facile with the energy barriers of 23 and 53 kJ/mol,

respectively. Therefore, the Mg₆MnO₈ with Li and W dopants that facilitate CH₃ dimerization and suppress CO formation can serve as an efficient catalytic oxygen carrier for CLOCM, which has been substantiated by the redox experiments shown in Figure 4.

Redox Stability of (Li,W)-Mg₆MnO₈. For a catalytic oxygen carrier to be commercially relevant in a CLOCM system, not only is it important for that oxygen carrier to achieve high productivity toward the C₂₊ hydrocarbon products but also it needs to display high stability in the chemical looping redox processes. Figure 9a shows the overall activity measured over the 15 s of OCM reaction time of the (Li,W)-codoped Mg₆MnO₈ oxygen carrier across 50 redox cycles. As depicted, the performance remained stable at 850 °C within a range of ±4% of the average value. This indicates that codoped samples possess high stability and good recyclability in the CLOCM system in addition to the high activity for the OCM reactions.

Panels (b) and (c) in Figure 9 are SEM images of (Li,W)-codoped Mg₆MnO₈ in its fresh form and 50 redox cycle aged form. Figure 9d is the cross section of the 50-cycle reacted sample, depicting the size of the pores present in the bulk. As seen from the SEM images, the sample does undergo an increase in the grain size, indicating a sintering tendency of the oxygen carrier upon redox cycles. This was further confirmed from the decrease in surface area of the 50-cycle reacted sample as compared to the fresh sample through the BET analysis mentioned in the Supporting Information. However, this sintering does not affect the CLOCM activity of the catalytic oxygen carrier as seen from Figure 9a. Additionally, XPS spectra were collected on the (Li,W)-Mg₆MnO₈ after 50 redox cycles and are depicted in Figure S5. As compared to the XPS spectra of the fresh (Li,W)-Mg₆MnO₈ sample, the peaks corresponding to Mg 1s, Mn 2p_{3/2}, and W 4f did not show a significant difference (within 0.1 eV). This further verifies the stability of (Li,W)-Mg₆MnO₈ over the 50 redox cycles. These results help establish the potential of this catalytic oxygen carrier for the CLOCM system and warrant further process and economic analysis.

■ CONCLUSION

This study demonstrated a strategy for designing a high performance codoped catalytic oxygen carrier for chemical looping oxidative coupling of methane. The goal of attaining this high performance would not only benefit the economic feasibility of the process but also aid in reducing the CO₂ footprint of the process. Here, codoping low concentrations of lithium and tungsten to the Mg₆MnO₈ oxygen carrier in chemical looping oxidative coupling of methane can dramatically enhance the C₂₊ yield and, thus, reduce the amount of CH₄ converted to CO₂, while maintaining the recyclability for 50 redox cycles. The redox experiments show that the codoped oxygen carrier (Li,W)-Mg₆MnO₈ achieves a C₂₊ yield of 28.6% at 850 °C in the absence of molecular oxygen, which is 80% higher than the combined yields of the Li-doped and W-doped Mg₆MnO₈. The codoping effect is also evident from the fact that the overall yield of the codoped catalytic oxygen carrier is 330% higher than that of the undoped Mg₆MnO₈. DFT calculations reveal that the W dopant leads to a higher oxygen vacancy formation energy than the undoped Mg₆MnO₈ and Li-doped Mg₆MnO₈. This stabilizes the surface lattice oxygen, reducing the CH₄ conversion in the system. The (Li,W)-codoped Mg₆MnO₈ regulates the oxygen formation energy through the interaction of the Li and W dopants on the catalytic oxygen carrier surface. Thus, the Li and W codoping induced active sites not only facilitate CH₃ dimerization but also inhibit CO₂ formation by suppressing the formation of unselective oxygen vacancies. Consequently, the C₂ yield is significantly enhanced due to this synergistic effect. These results indicate that the (Li,W)-codoped Mg₆MnO₈ is a promising catalytic oxygen carrier, showing commercial relevance for CLOCM and providing a catalytic dopant screening strategy for efficient chemical looping applications.

■ ASSOCIATED CONTENT

SI Supporting Information

The Supporting Information is available free of charge at <https://pubs.acs.org/doi/10.1021/acssuschemeng.0c07241>.

Details about the fixed bed setup as shown in Figure S1, equations for CH₄ conversion and C₂₊ selectivity depicted in eqs S1 and S2, DFT calculation details in eqs S3 and S4, dopant screening data as described in the text in Figures S2 and S3, XPS spectra of the W-doped Mg₆MnO₈ in Figure S4 and of the 50 redox cycle run (Li,W)-codoped Mg₆MnO₈ in Figure S5, and BET data of the fresh and 50 redox cycle run (Li,W)-codoped Mg₆MnO₈ (PDF)

■ AUTHOR INFORMATION

Corresponding Author

Liang-Shih Fan – Department of Chemical and Biomolecular Engineering, The Ohio State University, Columbus, Ohio 43210, United States; orcid.org/0000-0002-3892-5362; Email: fan.1@osu.edu

Authors

Deven S. Baser – Department of Chemical and Biomolecular Engineering, The Ohio State University, Columbus, Ohio 43210, United States; orcid.org/0000-0003-2658-2451

Zhuo Cheng – Department of Chemical and Biomolecular Engineering, The Ohio State University, Columbus, Ohio 43210, United States; orcid.org/0000-0001-7910-4264

Jonathan A. Fan – Department of Electrical Engineering, Ginzton Laboratory, Spilker Engineering and Applied Sciences, Stanford University, Stanford, California 94305, United States; orcid.org/0000-0001-9816-9979

Complete contact information is available at: <https://pubs.acs.org/doi/10.1021/acssuschemeng.0c07241>

Author Contributions

[§]D.S.B. and Z.C. contributed equally to this work.

Notes

The authors declare no competing financial interest.

■ ACKNOWLEDGMENTS

The service support provided by the Center for Electron Microscopy and the Analysis and NanoSystem Laboratory at The Ohio State University and the computing support provided by the Ohio Supercomputer Center are gratefully acknowledged.

■ REFERENCES

- (1) Fan, L.-S. *Chemical Looping Partial Oxidation: Gasification, Reforming, and Chemical Syntheses*; Cambridge University Press, 2017. DOI: 10.1017/9781108157841.
- (2) Kiani, D.; Sourav, S.; Baltrusaitis, J.; Wachs, I. E. Oxidative Coupling of Methane (OCM) by SiO₂-Supported Tungsten Oxide Catalysts Promoted with Mn and Na. *ACS Catal.* **2019**, 9 (7), 5912–5928.
- (3) Wood, D. A.; Nwaoha, C.; Towler, B. F. Gas-to-Liquids (GTL): A Review of an Industry Offering Several Routes for Monetizing Natural Gas. *J. Nat. Gas Sci. Eng.* **2012**, 9, 196–208.
- (4) Dong, L.; Wei, S.; Tan, S.; Zhang, H. GTL or LNG: Which Is the Best Way to Monetize “Stranded” Natural Gas? *Pet. Sci.* **2008**, 5 (4), 388–394.
- (5) Khalilpour, R.; Karimi, I. A. Evaluation of Utilization Alternatives for Stranded Natural Gas. *Energy* **2012**, 40 (1), 317–328.
- (6) Ojijigwo, E.; Oduzo, C. F.; Emekwuru, N. Economics of Gas to Wire Technology Applied in Gas Flare Management. *Eng. Sci. Technol. an Int. J.* **2016**, 19 (4), 2109–2118.
- (7) United Nations. *Transforming Our World: The 2030 Agenda for Sustainable Development*; Tech. Rep. A/RES/70/1; 2015.
- (8) United Nations. *United Nations Framework Convention on Climate Change, Paris Agreement*; 2015.
- (9) Chung, E. Y.; Wang, W. K.; Nadgouda, S. G.; Baser, D. S.; Sofranko, J. A.; Fan, L.-S. Catalytic Oxygen Carriers and Process Systems for Oxidative Coupling of Methane Using the Chemical Looping Technology. *Ind. Eng. Chem. Res.* **2016**, 55 (50), 12750–12764.
- (10) Puliyalil, H.; Lašić Jurković, D.; Dasireddy, V. D. B. C.; Likozar, B. A Review of Plasma-Assisted Catalytic Conversion of Gaseous Carbon Dioxide and Methane into Value-Added Platform Chemicals and Fuels. *RSC Adv.* **2018**, 8 (48), 27481–27508.
- (11) Fox, J. M. The Different Catalytic Routes for Methane Valorization: An Assessment of Processes for Liquid Fuels. *Catal. Rev.: Sci. Eng.* **1993**, 35 (2), 169–212.
- (12) Keller, G. E.; Bhasin, M. M. Synthesis of Ethylene via Oxidative Coupling of Methane. I. Determination of Active Catalysts. *J. Catal.* **1982**, 73 (1), 9–19.
- (13) Hammond, C.; Conrad, S.; Hermans, I. Oxidative Methane Upgrading. *ChemSusChem* **2012**, 5 (9), 1668–1686.
- (14) Ma, S.; Guo, X.; Zhao, L.; Scott, S.; Bao, X. Recent Progress in Methane Dehydroaromatization: From Laboratory Curiosities to Promising Technology. *J. Energy Chem.* **2013**, 22 (1), 1–20.

- (15) Jones, C. A.; Leonard, J. J.; Sofranko, J. A. Fuels for the Future: Remote Gas Conversion. *Energy Fuels* **1987**, *1* (1), 12–16.
- (16) Latimer, A. A.; Kakekhani, A.; Kulkarni, A. R.; Nørskov, J. K. Direct Methane to Methanol: The Selectivity-Conversion Limit and Design Strategies. *ACS Catal.* **2018**, *8*, 6894–6907.
- (17) Gesser, H. D.; Hunter, N. R.; Prakash, C. B. The Direct Conversion of Methane to Methanol by Controlled Oxidation. *Chem. Rev.* **1985**, *85* (4), 235–244.
- (18) Palkovits, R.; von Malotki, C.; Baumgarten, M.; Müllen, K.; Baltes, C.; Antonietti, M.; Kuhn, P.; Weber, J.; Thomas, A.; Schüth, F. Development of Molecular and Solid Catalysts for the Direct Low-Temperature Oxidation of Methane to Methanol. *ChemSusChem* **2010**, *3* (2), 277–282.
- (19) Li, N.; Jiang, R.; Li, Y.; Zhou, J.; Ma, Q.; Shen, S.; Liu, M. Plasma-Assisted Photocatalysis of CH₄ and CO₂ into Ethylene. *ACS Sustainable Chem. Eng.* **2019**, *7* (13), 11455–11463.
- (20) Yunarti, R. T.; Gu, S.; Choi, J. W.; Jae, J.; Suh, D. J.; Ha, J. M. Oxidative Coupling of Methane Using Mg/Ti-Doped SiO₂-Supported Na₂WO₄/Mn Catalysts. *ACS Sustainable Chem. Eng.* **2017**, *5* (5), 3667–3674.
- (21) Sinev, M. Y.; Fattakhova, Z. T.; Lomonosov, V. I.; Gordienko, Y. A. Kinetics of Oxidative Coupling of Methane: Bridging the Gap between Comprehension and Description. *J. Nat. Gas Chem.* **2009**, *18* (3), 273–287.
- (22) Zavyalova, U.; Holena, M.; Schlögl, R.; Baerns, M. Statistical Analysis of Past Catalytic Data on Oxidative Methane Coupling for New Insights into the Composition of High-Performance Catalysts. *ChemCatChem* **2011**, *3* (12), 1935–1947.
- (23) Su, Y. S.; Ying, J. Y.; Green, W. H. Upper Bound on the Yield for Oxidative Coupling of Methane. *J. Catal.* **2003**, *218* (2), 321–333.
- (24) Parishan, S.; Littlewood, P.; Arinchtin, A.; Fleischer, V.; Schomäcker, R. Chemical Looping as a Reactor Concept for the Oxidative Coupling of Methane over the Mn_xO_y-Na₂WO₄/SiO₂ Catalyst, Benefits and Limitation. *Catal. Today* **2018**, *311*, 40–47.
- (25) Cruellas, A.; Bakker, J. J.; van Sint Annaland, M.; Medrano, J. A.; Gallucci, F. Techno-Economic Analysis of Oxidative Coupling of Methane: Current State of the Art and Future Perspectives. *Energy Convers. Manage.* **2019**, *198*, 111789.
- (26) Cruellas, A.; Melchiori, T.; Gallucci, F.; van Sint Annaland, M. Advanced Reactor Concepts for Oxidative Coupling of Methane. *Catal. Rev.: Sci. Eng.* **2017**, *59* (3), 234–294.
- (27) Lunsford, J. H. The Catalytic Oxidative Coupling of Methane. *Angew. Chem., Int. Ed. Engl.* **1995**, *34* (9), 970–980.
- (28) Edwards, J. H.; Do, K. T.; Tyler, R. J. The OXCO Process. A New Concept for the Production of Olefins from Natural Gas. *Fuel* **1992**, *71* (3), 325–334.
- (29) Zeng, L.; Cheng, Z.; Fan, J. A.; Fan, L.-S.; Gong, J. Metal Oxide Redox Chemistry for Chemical Looping Processes. *Nat. Rev. Chem.* **2018**, *2* (11), 349–364.
- (30) Baser, D. S.; Nadgouda, S. G.; Joshi, A. S.; Fan, L.-S. 110th Anniversary: Indirect Partial Oxidation of Methane Using a Counter-Current Moving-Bed Chemical Looping Configuration for Enhanced Syngas Production. *Ind. Eng. Chem. Res.* **2019**, *58* (36), 16407–16416.
- (31) Godini, H. R.; Xiao, S.; Jašo, S.; Stünkel, S.; Salerno, D.; Son, N. X.; Song, S.; Wozny, G. Techno-Economic Analysis of Integrating the Methane Oxidative Coupling and Methane Reforming Processes. *Fuel Process. Technol.* **2013**, *106*, 684–694.
- (32) Fleischer, V.; Littlewood, P.; Parishan, S.; Schomäcker, R. Chemical Looping as Reactor Concept for the Oxidative Coupling of Methane over a Na₂WO₄/Mn/SiO₂ Catalyst. *Chem. Eng. J.* **2016**, *306*, 646–654.
- (33) Beck, B.; Fleischer, V.; Arndt, S.; Hevia, M. G.; Urakawa, A.; Hugo, P.; Schomäcker, R. Oxidative Coupling of Methane—A Complex Surface/Gas Phase Mechanism with Strong Impact on the Reaction Engineering. *Catal. Today* **2014**, *228*, 212–218.
- (34) Luo, L.; Tang, X.; Wang, W.; Wang, Y.; Sun, S.; Qi, F.; Huang, W. Methyl Radicals in Oxidative Coupling of Methane Directly Confirmed by Synchrotron VUV Photoionization Mass Spectroscopy. *Sci. Rep.* **2013**, *3* (1), 1625.
- (35) Choudhary, V. R.; Rane, V. H. Acidity/Basicity of Rare-Earth Oxides and Their Catalytic Activity in Oxidative Coupling of Methane to C₂-Hydrocarbons. *J. Catal.* **1991**, *130* (2), 411–422.
- (36) Schwach, P.; Willinger, M. G.; Trunschke, A.; Schlögl, R. Methane Coupling over Magnesium Oxide: How Doping Can Work. *Angew. Chem., Int. Ed.* **2013**, *52* (43), 11381–11384.
- (37) Ruckenstein, E.; Khan, A. Z. Synergistic Effect of Bialkali Metal Chlorides Promoted Magnesia on Oxidative Coupling of Methane. *Catal. Lett.* **1993**, *18* (1), 27–35.
- (38) Arndt, S.; Laugel, G.; Levchenko, S.; Horn, R.; Baerns, M.; Scheffler, M.; Schlögl, R.; Schomäcker, R. A Critical Assessment of Li/MgO-Based Catalysts for the Oxidative Coupling of Methane. *Catal. Rev.: Sci. Eng.* **2011**, *53* (4), 424–514.
- (39) Dedov, A. G.; Loktev, A. S.; Moiseev, I. I.; Aboukais, A.; Lamonnier, J.-F.; Filimonov, I. N. Oxidative Coupling of Methane Catalyzed by Rare Earth Oxides: Unexpected Synergistic Effect of the Oxide Mixtures. *Appl. Catal., A* **2003**, *245* (2), 209–220.
- (40) Wang, P.; Zhao, G.; Wang, Y.; Lu, Y. MnTiO₃-Driven Low-Temperature Oxidative Coupling of Methane over TiO₂-Doped Mn₂O₃-Na₂WO₄/SiO₂. *Sci. Adv.* **2017**, *3* (6), e1603180.
- (41) Palermo, A.; Holgado Vazquez, J. P.; Lambert, R. M. New Efficient Catalysts for the Oxidative Coupling of Methane. *Catal. Lett.* **2000**, *68* (3), 191–196.
- (42) Yu, Z. Q.; Yang, X. M.; Lunsford, J. H.; Rosynek, M. P. Oxidative Coupling of Methane over Na₂WO₄/CeO₂ and Related Catalysts. *J. Catal.* **1995**, *154* (1), 163–173.
- (43) Maitra, A. M.; Sacchetta, C.; Tyler, R. J. Effect of Feed Dilution with Helium and Steam on Catalytic Oxidative Coupling of Methane (OCM). In *Natural Gas Conversion II*; Curry-Hyde, H. E., Howe, R. F., Eds.; Studies in Surface Science and Catalysis, Vol. 81; Elsevier, 1994; pp 261–263. DOI: 10.1016/S0167-2991(08)63876-8.
- (44) Godini, H. R.; Trivedi, H.; de Villasante, A. G.; Görke, O.; Jašo, S.; Simon, U.; Berthold, A.; Witt, W.; Wozny, G. Design and Demonstration of an Experimental Membrane Reactor Set-up for Oxidative Coupling of Methane. *Chem. Eng. Res. Des.* **2013**, *91* (12), 2671–2681.
- (45) Sofranko, J. A.; Leonard, J. J.; Jones, C. A.; Gaffney, A. M.; Withers, H. P. Catalytic Oxidative Coupling of Methane over Sodium-Promoted Mn/SiO₂ and Mn/MgO. *Catal. Today* **1988**, *3* (2), 127–135.
- (46) Sung, J. S.; Choo, K. Y.; Kim, T. H.; Greish, A.; Glukhov, L.; Finashina, E.; Kustov, L. Peculiarities of Oxidative Coupling of Methane in Redox Cyclic Mode over Ag–La₂O₃/SiO₂ Catalysts. *Appl. Catal., A* **2010**, *380* (1–2), 28–32.
- (47) Fleischer, V.; Simon, U.; Parishan, S.; Colmenares, M. G.; Görke, O.; Gurlo, A.; Riedel, W.; Thum, L.; Schmidt, J.; Risse, T.; et al. Investigation of the Role of the Na₂WO₄/Mn/SiO₂ Catalyst Composition in the Oxidative Coupling of Methane by Chemical Looping Experiments. *J. Catal.* **2018**, *360*, 102–117.
- (48) Greish, A. A.; Glukhov, L. M.; Finashina, E. D.; Kustov, L. M.; Sung, J.-S.; Choo, K.-Y.; Kim, T.-H. Oxidative Coupling of Methane in the Redox Cyclic Mode over the Catalysts on the Basis of CeO₂ and La₂O₃. *Mendeleev Commun.* **2010**, *20* (1), 28–30.
- (49) Gaffney, A. M.; Jones, C. A.; Leonard, J. J.; Sofranko, J. A. Oxidative Coupling of Methane over Sodium Promoted Praseodymium Oxide. *J. Catal.* **1988**, *114* (2), 422–432.
- (50) Cheng, Z.; Baser, D. S.; Nadgouda, S. G.; Qin, L.; Fan, J. A.; Fan, L.-S. C₂ Selectivity Enhancement in Chemical Looping Oxidative Coupling of Methane over a Mg–Mn Composite Oxygen Carrier by Li-Doping-Induced Oxygen Vacancies. *ACS Energy Lett.* **2018**, *3* (7), 1730–1736.
- (51) Ioffe, L. M.; Bosch, P.; Viveros, T.; Sanchez, H.; Borodko, Y. G. Natural Manganese Oxides as Catalysts for Oxidative Coupling of Methane: A Structural and Degradation Study. *Mater. Chem. Phys.* **1997**, *51* (3), 269–275.

- (52) Qin, L.; Cheng, Z.; Baser, D.; Goldenbaum, T.; Fan, J. A.; Fan, L.-S. Cyclic Redox Scheme towards Shale Gas Reforming: A Review and Perspectives. *React. Chem. Eng.* **2020**, *5* (12), 2204–2220.
- (53) Yusuf, S.; Neal, L.; Bao, Z.; Wu, Z.; Li, F. Effects of Sodium and Tungsten Promoters on Mg₆MnO₈-Based Core–Shell Redox Catalysts for Chemical Looping—Oxidative Dehydrogenation of Ethane. *ACS Catal.* **2019**, *9* (4), 3174–3186.
- (54) Kresse, G.; Furthmüller, J. Efficiency of Ab-Initio Total Energy Calculations for Metals and Semiconductors Using a Plane-Wave Basis Set. *Comput. Mater. Sci.* **1996**, *6* (1), 15–50.
- (55) Kresse, G.; Furthmüller, J. Efficient Iterative Schemes for Ab Initio Total-Energy Calculations Using a Plane-Wave Basis Set. *Phys. Rev. B: Condens. Matter Mater. Phys.* **1996**, *54* (16), 11169–11186.
- (56) Perdew, J. P.; Burke, K.; Ernzerhof, M. Generalized Gradient Approximation Made Simple. *Phys. Rev. Lett.* **1996**, *77* (18), 3865–3868.
- (57) Van Geem, K. M.; Heynderickx, G. J.; Marin, G. B. Effect of Radial Temperature Profiles on Yields in Steam Cracking. *AIChE J.* **2004**, *50* (1), 173–183.
- (58) Biesinger, M. C.; Payne, B. P.; Grosvenor, A. P.; Lau, L. W. M.; Gerson, A. R.; Smart, R. S. C. Resolving Surface Chemical States in XPS Analysis of First Row Transition Metals, Oxides and Hydroxides: Cr, Mn, Fe, Co and Ni. *Appl. Surf. Sci.* **2011**, *257* (7), 2717–2730.
- (59) Alov, N. V. Determination of the States of Oxidation of Metals in Thin Oxide Films by X-Ray Photoelectron Spectroscopy. *J. Anal. Chem.* **2005**, *60* (5), 431–435.
- (60) Henkelman, G.; Uberuaga, B. P.; Jónsson, H. A Climbing Image Nudged Elastic Band Method for Finding Saddle Points and Minimum Energy Paths. *J. Chem. Phys.* **2000**, *113* (22), 9901–9904.